Computers in Biology and Medicine 81 (2017) 121–129

Contents lists available at ScienceDirect

Computers in Biology and Medicine

journal homepage: www.elsevier.com/locate/compbiomed

An advanced MRI and MRSI data fusion scheme for enhancing unsupervised brain tumor differentiation

Yuqian Li[a,*], Xin Liu[a], Feng Wei[a], Diana M. Sima[b], Sofie Van Cauter[c,d], Uwe Himmelreich[e], Yiming Pi[a], Guang Hu[f], Yi Yao[g], Sabine Van Huffel[b]

[a] School of Electronic Engineering, University of Electronic Science and Technology of China, Chengdu, China
[b] STADIUS Centre for Dynamical Systems, Signal Processing and Data Analytics, Department of Electrical Engineering (ESAT), KU Leuven, Leuven, Belgium
[c] Department of Radiology, KU Leuven, Leuven, Belgium
[d] Ziekenhuizen Oost Limburg, Genk, Belgium
[e] Department of Imaging and Pathology, KU Leuven, Leuven, Belgium
[f] Center for Systems Biology, School of Electronic and Information Engineering, Soochow University, Suzhou, China
[g] School of Communication and Information Engineering, University of Electronic Science and Technology of China, Chengdu, China

ARTICLE INFO

Keywords:
Data fusion
Magnetic resonance spectroscopic imaging (MRSI)
Magnetic resonance imaging (MRI)
Non-negative matrix factorization (NMF)

ABSTRACT

Proton Magnetic Resonance Spectroscopic Imaging (^{1}H MRSI) has shown great potential in tumor diagnosis since it provides localized biochemical information discriminating different tissue types, though it typically has low spatial resolution. Magnetic Resonance Imaging (MRI) is widely used in tumor diagnosis as an in vivo tool due to its high resolution and excellent soft tissue discrimination. This paper presents an advanced data fusion scheme for brain tumor diagnosis using both MRSI and MRI data to improve the tumor differentiation accuracy of MRSI alone. Non-negative Matrix Factorization (NMF) of the spectral feature vectors from MRSI data and the image fusion with MRI based on wavelet analysis are implemented jointly. Hence, it takes advantage of the biochemical tissue discrimination of MRSI as well as the high resolution of MRI. The feasibility of the proposed frame work is validated by comparing with the expert delineations, giving mean correlation coefficients for the tumor source of 0.97 and the Dice score of tumor region overlap of 0.90. These results compare favorably against those obtained with a previously proposed NMF method where MRSI and MRI are integrated by stacking the MRSI and MRI features.

1. Introduction

The concept of data fusion refers to data integration using different sources and has as objective to provide better identification or differentiation of an underlying object. Proper choice of fusion scheme usually highly depends upon the application and the data structure. With the development of medical imaging technologies, the appeal of robust analysis using information from different modalities is getting stronger for more reliable diagnosis [1,2]. However, biomedical data fusion, especially for data that has different characteristics, is not a trivial task that can be solved by generic image fusion algorithms. It is important to develop advanced fusion methods that are tuned to the requirements of specific clinical problem and that take into account the advantages and limitations of the selected data modalities.

Glioma is the most common primary brain tumor in adults according to the World Health Organization (WHO) criteria [3]. Low-grade glioma shows better prognosis [4] than the high-grade glioma, but could still be life-threatening if not properly controlled. Early detection and localization of gliomas is of most importance in surgery planning and treatment monitoring. Conventional Magnetic Resonance Imaging (MRI) has excellent soft tissue contrast and has become an established in vivo tool for primary detection and assessment of brain gliomas. However, due to intratumoral heterogeneity, brain tumors are sometimes not adequately reflected in conventional MRI. The evaluation of lesions on conventional MRI can either under- or overestimate the presence of active tumor [5]. The sensitivity and specificity of tumor typing and grading is also limited due to difficulties in distinguishing between tumor, edema, and nonspecific treatment effects [6,7].

Proton magnetic resonance spectroscopic imaging (^{1}H MRSI) data provides metabolic information of the tissue within the selected 2D or 3D volume of interest (VOI) [8], but it has poor spatial resolution (e.g., voxel size: ~1 cm^3). The concentration level of certain metabolites that can be estimated from ^{1}H MRSI may give an indication regarding

* Corresponding author.
E-mail address: yuqianli@uestc.edu.cn (Y. Li).

http://dx.doi.org/10.1016/j.compbiomed.2016.12.017
Received 6 September 2016; Received in revised form 9 December 2016; Accepted 26 December 2016
0010-4825/ © 2016 Elsevier Ltd. All rights reserved.

tumor type, grade or infiltration. Nosologic imaging [9,10] and many related methods [11–17] using MRSI data have been developed for tumor tissue differentiation and more easily interpretable visualization. But their application in clinical practice is still not spread widely, which is in part due to the low sensitivity of MRSI, making the technique suffer from the low spatial resolution. Thus, the sufficient description of the tumor edges and the detailed tumor tissues is impossible through MRSI alone. Image interpolation of the spatial distribution map may artificially increase the resolution. However, since gliomas can be infiltrative, simple interpolation hides relevant details.

Emerging interest has been shown towards the methods that increase the accuracy of tumor tissue differentiation by combining several different modalities [18–24]. One of the most common ways to integrate MRSI with other modalities is to extract a metabolite-based distribution map and overlay it semi-transparently on other image modalities for the experts to perform manual delineation. No real data/image fusion or automatic tumor differential happens in such cases [22–24]. Typically, data fusion methods [18,19,21] perform *early integration*, i.e., they stack the data from different modalities into common feature vectors before applying source separation or classification algorithms. By treating all data types equally, the intrinsic characteristics of the data, such as image resolution, contrast, edge sharpness and level of detail, might be ignored.

Recently, non-negative matrix factorization (NMF) [25], a blind source separation method capable of extracting source-based representation, has shown promising results in MRSI-based nosologic imaging of brain tumors [10,14–17,19,26]. The cost function of NMF problems are usually minimized by updating the tissue-specific sources and the weights (herein, the distribution maps) in an *iterative* manner to find a local minimum. In the area of remote sensing, a data fusion algorithm based on NMF, namely coupled NMF, has been successfully applied in multi-scale and multi-resolution data fusion [27]. It applied NMF on both low spatial resolution hyperspectral data and high spatial resolution multi-spectral data, and recovered the sources by alternately unmixing the distribution maps of the two data types within each inner iteration of NMF. In contrast to early integration, this approach implements a fusing mechanism that explicitly takes into account the different spatial resolutions of the two datasets. Nevertheless, this approach requires that both datasets are multi-parametric and that source separation of each dataset separately is meaningful.

In this paper, we focus on developing an MRSI and MRI fusion scheme for brain tumor differentiation inspired by the coupled NMF method [27]. The goal is to increase the tumor discriminative capability of MRSI signals by fusing with the more detailed structural information from MRI. MRSI data in the form of multi-variate signals also makes itself decomposable by NMF algorithms, thus it is taken as the main stream of tumor tissue differentiation. The detailed structural information from the MR image is added iteratively as the fusion part for improving the whole resolution of the tumor distribution map. Specifically, within each iterative updating of the NMF algorithm, the tissue specific distribution maps obtained from the decomposition of MRSI data are fused with the high resolution MR image using an image fusion technique based on wavelet analysis. Then, the fusion results are used as new distribution maps to update the sources and continue with the iterative updating of NMF. The NMF updating step and image fusion step are combined and repeated until a stopping criterion is met. In this way, the detailed tumor tissue information from MRI is added to the distribution maps of MRSI data, without losing the biochemical information provided by MRSI. Experimental results demonstrate the performance of the proposed fusion scheme in comparison with early integration NMF, i.e., the case when NMF is applied on stacked MRSI and MRI feature.

2. Methodology

2.1. Materials

Seven patients with low grade glioma (LGG) based on conventional radiological imaging were enrolled for this study. The lesions were classified according to grade using the 2007 WHO classification [3]. The institutional human ethics review board approved this study. Written informed consent was obtained from every patient before participation.

2.2. Data acquisition and preprocessing

MRI acquisition was performed on a 3T MR system (Philips Achieva, Best, the Netherlands) using a body coil for transmission and an eight-channel head coil for signal reception.

2.2.1. Conventional MRI

Axial spin echo T2-weighted MRI was acquired with the following parameters, TR/TE=3000/80 ms; slice/gap, 4/1 mm; turbo factor, 10; field of view (FOV), 230 mm×184 mm; acquisition matrix, 400×300. The original resolution level was 0.98 mm×0.98 mm×1 mm. Geometric matching between MRI and MRSI is performed using the coordinates of the two systems. Only the MRI slices coinciding with the central plane of the MRSI VOI and the regions corresponding to the MRSI region of interest (ROI) were considered for the data fusion. Delineation of active tumor area for each patient was performed manually by a neuro-radiologist (with 6 years of experience in brain tumor research) on the basis of visual inspection of the MRI data, using the medical image viewer MRIcro. Regions comprising non-contrast-enhancing tumor were delineated on the T2-weighted images. The delineated tumor area is used as the ground truth for validating resulting distribution map.

2.2.2. MRSI data

A two-dimensional ^{1}H MRSI protocol was used as described previously [28]. In brief, a point-resolved spectroscopy sequence was used as the volume selection technique with a bandwidth of 1.3 kHz for the conventional slice-selective pulses; TR/TE, 2000/35 ms; FOV, 160 mm×160 mm; maximal VOI, 80 mm×80 mm; slice thickness, 10 mm; acquisition voxel size, 10 mm×10 mm; reconstruction voxel size, 5 mm×5 mm; receiver bandwidth, 2000 Hz; acquired data points, 2048; number of signal averages, 1; water suppression method, multiple optimizations insensitive suppression train [29]; first- and second-order pencil beam shimming; parallel imaging, sensitivity encoding with reduction factors of 2 (left–right) and 1.8 (anterior–posterior); scan time, 3 min 30 s. Automated pre-scanning optimized the shim in order to yield a peak width consistently under 20 Hz full width at half maximum (FWHM). The slice was positioned in the center of the tumor.

The raw MRSI data were exported from the Philips platform and spatially aligned after standard post-processing (zero filling in k-space, transformation from k-space to spatial domain, automatic phase correction and eddy current correction). (Pre-)processing including water filtering and alignment was performed with SPID [30] in Matlab 2012b (MathWorks, Natick, MA, USA) as previously reported [26]. A band of voxels at the outer edges of the ROI was omitted to avoid chemical shift displacement artifacts and lipid contamination. After choosing the ROI, quantified metabolites (as listed in Table 1) for each voxel within the ROI are generated using peak integration as a *metabolite feature vector* of MRSI data for data fusion. In the end, the MRSI *metabolite features* within ROI were spatially resampled using linear interpolation to be scaled to the same size of MRI voxels, i.e. 0.98×0.98×1 mm^3.

All the tumor voxels are labeled tissue-specifically by the neuro-radiologist. The labeling is performed by visual inspection of the

Table 1
Metabolites and peak integration range.

Metabolites	Metabolites abbreviation	Integration range (ppm)
Creatine	Cre 1	3.90–4.09
Glutamine+Glutamate	Glx 1	3.75–3.85
myo-inositol	Myo	3.54–3.64
Choline	Cho	3.17–3.27
Creatine	Cre2	3.02–3.12
Glutamine+Glutamate	Glx2	2.20–2.46
N-acetylaspartate	NAA	1.98–2.08
alanine	Ala	1.30–1.50
lactate+Lipid	Lac-Lip1	1.10–1.50
Lipid	Lip1	1.25–1.35
Lipid	Lip2	0.80–0.95

spectra from all voxels within ROI. Reference spectra for each individual patient are generated by averaging the tumor spectra from all labeled voxels. Then a reference feature vector containing 11 integrated values for each patient is obtained using the same peak integration intervals as shown in Table 1. This feature vector is used as the ground truth of tumor feature source to calculate the correlation coefficients in Table 2 to validate the accuracy of obtained features sources.

2.3. NMF model for MRSI data decomposition

Given a data set $\mathbf{X}$ from the ROI of MRSI data, each column of $\mathbf{X}$ represents a *metabolite feature vector* from one MRSI voxel after resampling to MRI resolution spatially, i.e., each column of $\mathbf{X}$ contains 11 points representing the 11 metabolite features listed in Table 1. $\mathbf{X}$ can be blindly separated into a source matrix $\mathbf{W}$ and a distribution matrix $\mathbf{H}$:

$$\mathbf{X}_{m\times n} \approx \mathbf{W}_{m\times r} \times \mathbf{H}_{r\times n}$$
$$s.t. \quad \mathbf{W},\ \mathbf{H} \geq 0 \tag{1}$$

where r is the number of sources. For data of LGG patients, we aim to differentiate the brain tissue into tumor and normal tissue. Therefore, the number of sources r is set to be 2. Each column of $\mathbf{W}$ represents the metabolite feature vector of one source and each row of $\mathbf{H}$ contains all the weights of the corresponding source for each voxel. Here, the two column of $\mathbf{W}$ represent the metabolite feature vector of tumor and normal tissue, respectively. The spatial distribution map of each source (here, normal tissue or tumor tissue) can be obtained by reshaping each row of $\mathbf{H}$ back to the shape of the MRSI ROI. So two distribution maps are obtained, one as the tumor distribution map and the other as the distribution map for normal tissue. These two distribution maps are complementary to each other. In the tumor distribution map, the high intensities/weights represent the tumor. In the normal distribution map, the high intensities/weights represent the normal tissue. This NMF problem is usually solved by *iteratively* updating $\mathbf{W}$ and $\mathbf{H}$. Several NMF implementations are available in the literature, but the specific choice is not essential for the proposed fusion framework. For our experimental results, hierarchical alternating least squares (HALS) [31] is chosen as the NMF algorithm since it has shown good performance in our previous work [32].

2.4. Multi-modality fusion framework for MRSI and MRI

In order to improve the spatial resolution of the tumor tissue distribution derived from MRSI, we incorporate more detailed information from MRI into the inner iteration procedure of NMF. Within each NMF inner iteration t, image fusion is performed between MRI and the distribution maps of MRSI $\mathbf{H}^{(t)}$ (where t represents for the iteration number within the NMF algorithm). As described in Section 2.3, two distribution maps (i.e. one for tumor and one for normal tissue) are obtained as the derivatives during MRSI decomposition. Since the brain lesions show high intensities on the T2-weighted MRI images, we use the T2-weighted MRI image $\mathbf{I}$ to fuse with the tumor distribution map and use the complement image $\bar{\mathbf{I}}$) to fuse with the distribution map of the tissue. The obtained two new distribution maps, one for tumor and one for normal tissue, are then reshaped into rows of the new distribution matrix $\mathbf{H}^{(t)}_{new}$ which is used to update the source matrix $\mathbf{W}^{(t)}$. In turn, when the new $\mathbf{W}^{(t+1)}$ is obtained, it is used to update the $\mathbf{H}^{(t+1)}$ which is then fused with MRI again. This procedure continues in the NMF inner iterations until a stopping criterion is met. The fusion scheme is shown in Fig. 1(a). The block of "Image fusion" is explained in detail later on (Fig. 2 and Section 2.5).

Sources obtained by applying NMF on MRSI data only using Eq. (1) are used as the initial values for the proposed NMF fusion scheme. The following convergence condition is used as the stopping criterion with a given small threshold $\varepsilon = 10^{-3}$,

$$\|\mathbf{W}^{(t+1)} - \mathbf{W}^{(t)}\|_F^2 \leq \varepsilon \tag{2}$$

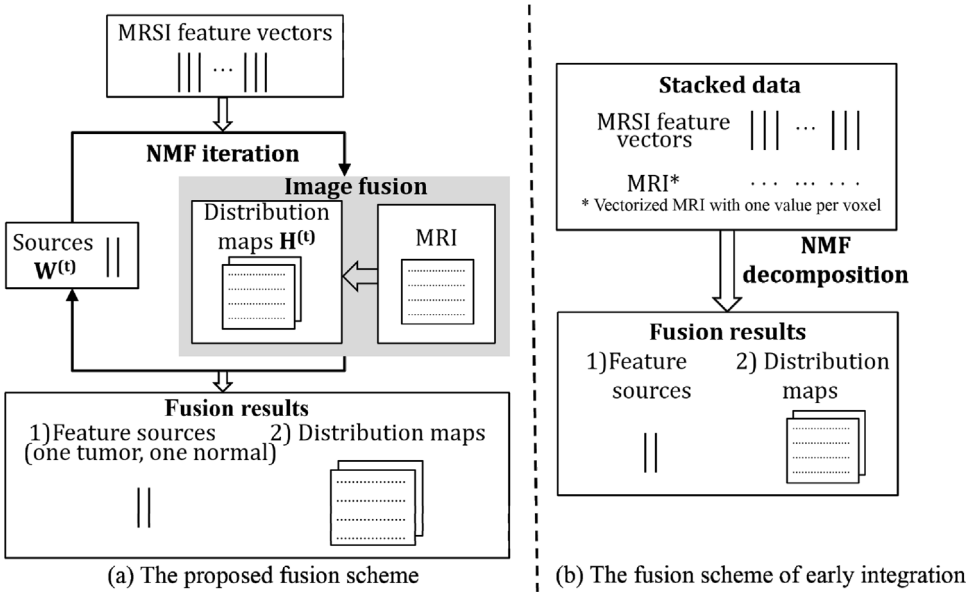


Fig. 1. Fusion scheme. Each vertical line for MRSI represents for one metabolite feature vector. Each dot point for MRI represents for the value of each MRI voxel.

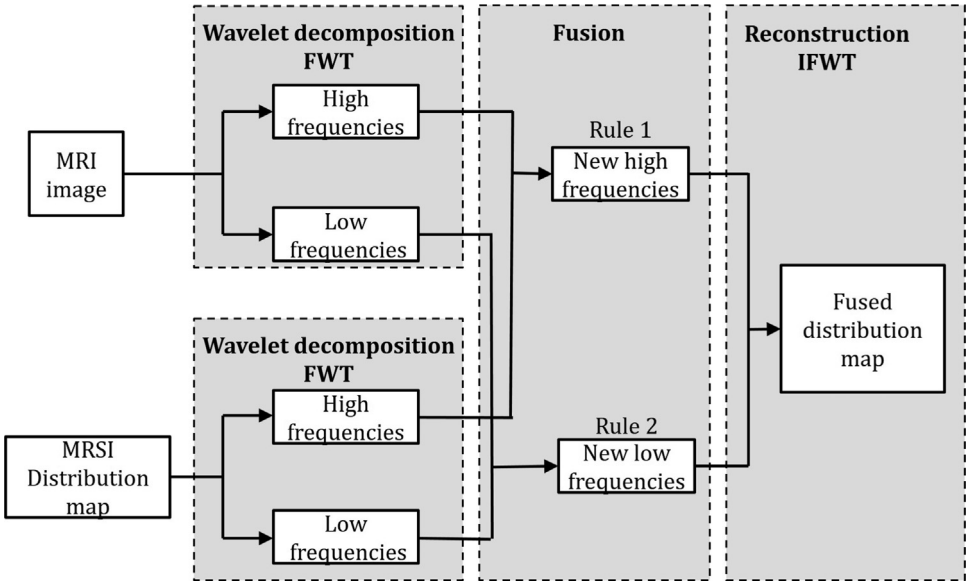


Fig. 2. Workflow of the image fusion step based on wavelet decomposition.

where t represents for the index of NMF iteration. Minimum iteration number is set to 200 in order to guarantee enough iterations involving image fusion. Additionally, a predefined maximum iteration number (500 times) is added in case that the above convergence condition is not met.

2.5. Image fusion based on wavelet decomposition

The fast wavelet decomposition (FWT) and reconstruction (IFWT) algorithm developed by Mallat [33] in 1988 is one of the most popular wavelet decomposition methods. Applying FWT to an image produces approximation coefficients (called low frequencies) that present edge information and detail coefficients (called high frequencies) that present the more detailed image information. In view of these properties, we use FWT to extract high and low frequencies from images of different types for fusion and then use the fused frequencies to reconstruct the new images using IFWT. Fig. 2 illustrates the image fusion between MRSI distribution map (either tumor or normal distribution map) and MRI image (either $\mathbf{I}$ or the complement image $\bar{\mathbf{I}}$, correspondingly) without loss of generality. Within each NMF inner iteration t of the MRSI data decomposition, we apply FWT to both the MRI image and the distribution map to obtain both the high frequencies and low frequencies from both image type. Then the high frequencies generated from MRI $\mathbf{I}_H$ and the high frequencies generated from the MRSI distribution map $\mathbf{H}_H$ are fused using the fusion rule described in Section 2.5.1. The low frequencies generated from MRI $\mathbf{I}_L$ and the low frequencies generated from MRSI distribution map $\mathbf{H}_L$ are fused using another fusion rule, as described in Section 2.5.2. Then, the fused high frequencies and low frequencies obtained from the wavelet domain are used to reconstruct a new spatial distribution map in the image domain using IFWT. By applying this image fusion step for tumor and normal image, two new distribution maps (one for tumor and one for normal tissue) are obtained to reform a new distribution matrix $\mathbf{H}_{new}^{(t)}$, which is further used to continue the NMF inner iteration. For the image decomposition based on wavelet, two decomposition levels and "symlet 4" wavelet are used in both cases to illustrate our approach in the experimental results. The work flow of this image fusion step based on wavelet decomposition is shown in Fig. 2.

2.5.1. Fusion rule for the low frequencies based on fuzzy adaptive weights

In order to develop reasonable criteria for fusing the low frequencies $\mathbf{H}_L$ obtained from the wavelet decomposition of the MRSI distribution map with the low frequencies $\mathbf{I}_L$ obtained from the wavelet decomposition of the MR image, we propose to use adaptive weights based on the Fuzzy Gaussian Membership Function:

$$\mathbf{F}_L(i,j) = \eta_0(i,j)\mathbf{I}_L(i,j) + \eta_1(i,j)\mathbf{H}_L(i,j) \tag{3}$$

Where (i,j) indicates the location where the fusion of low frequency components takes place; η_0 and η_1 are the adaptive weights with constraint $\eta_0(i,j) + \eta_1(i,j) = 1$. The Gaussian Membership Function (MF) is used for defining the fuzzy adaptive weights for η_0:

$$\eta_0(i,j) = \exp[-\frac{(\mathbf{H}_L(i,j) - \mu)^2}{2\sigma^2}] \tag{4}$$

where the mean of $\mathbf{H}_L$, μ, represents the MF's center. The standard deviation determines the width of the MF. η_0 takes big value near the tumor edge and small values far away from the tumor edge. In such a case, MRI has higher weight than MRSI at regions near the tumor edge and vice versa.

2.5.2. Fusion rule for the high frequencies

The high frequency components of the MR image contain detailed information such as texture, tumor heterogeneity, etc. In order to preserve the detailed information from both the MRI and the distribution map of MRSI as much as possible, we take the maximum value of the two,

$$\begin{aligned} &\mathbf{F}_H^{(t)}(i,j) = \max(\mathbf{I}_H(i,j), \quad \mathbf{H}_H{}^{(t)}(i,j)) \\ &s.t. \quad \mathbf{I}_H(i,j) > 0, \quad \mathbf{H}_H{}^{(t)}(i,j) > 0 \end{aligned} \tag{5}$$

where $\mathbf{I}_H$ and $\mathbf{H}_H$ are the high frequency components of MRI and the spatial distribution maps of MRSI, respectively; (i,j) is the voxel index of the location where this fusion rule is applied;

2.6. Results analysis and methods comparison

To evaluate the proposed fusion scheme, we compare our results with expert labeling and delineations, but also with the early integration method, which directly performs NMF on the stacked features

from MRI and MRSI (see Fig. 1(b)). The accuracy of the recovered feature source are measured using the correlation coefficients with reference feature sources for each patient (see Section 2.6.1). The accuracy of the spatial distribution is measured using the Dice score (see Section 2.6.2).

2.6.1. Validation using correlation coefficients

The correlation coefficient of two random variables **a** and **b** is a measure of their linear dependence:

$$corr(\mathbf{a}, \mathbf{b}) = \frac{(\mathbf{a} - \bar{\mathbf{a}})^T (\mathbf{b} - \bar{\mathbf{b}})}{\|\mathbf{a} - \bar{\mathbf{a}}\| \cdot \|\mathbf{b} - \bar{\mathbf{b}}\|} \quad (6)$$

where $\bar{\mathbf{a}}$ and $\bar{\mathbf{b}}$ are the means of **a** and **b**, respectively. Here, we use it to measure the similarity of the recovered feature sources and the reference feature sources. The reference spectra is generated by averaging the spectra from all the tumor voxels labeled as normal or tumor by the radiologist. The averaged reference spectra are then peak integrated as described in Section 2.2 in order to obtain the reference feature sources of the same length as the recovered sources.

2.6.2. Validation using Dice score

Dice score [34] is used to evaluate the accuracy of the tumor region determined using the proposed fusion method. The tumor distribution map needs to be binarized for this purpose. To this end, we use k-means clustering with 2 clusters on the set of values pertaining to the normal and tumor tissue distribution maps. Then the tumor region is compared with the manual segmentation by the experienced radiologist.

$$Dice = 2 \times \frac{A_{fusion} \cap A_{radiol}}{A_{fusion} + A_{radiol}} \quad (7)$$

where A_{fusion} is the region defined by the proposed fusion scheme and A_{radiol} is the region defined by the radiologist. Similarly, we generate tumor segmentations from the tumor tissue distribution maps obtained with the early integration method for methods comparison.

3. Experimental results

3.1. Fusion results for spatial distribution

The fusion results are shown in Fig. 3 on seven low grade glioma patients. The color maps are the spatial distribution of tumor regions with red color indicating tumor area. As fusion results shown in the 4th column for each patient, by fusing with MR images, more detailed information is added to the tumor regions (the red area) than the tumor regions which is only determined by MRSI as shown in the 3rd column. The regions which could not be decided by MRSI only (the black regions in the 3rd column) are indicated to be tumor or normal tissue after fusing with MRI. The tumor differentiation results of our fusion method (the red regions in the 4th column) are compared with the expert delineation of active tumor indicated by the black lines. In most cases, the tumor regions produced by our method are consistent with the expert delineation. The main difference (as shown in patient 4 and 7) may come from the CSF which presents a similar hyperintense contrast as tumor tissue in the T2-weighted image used as conventional MRI. Further investigation and analysis about these differences will be shown in Section 3.3.

Fig. 3, 2nd column, shows the tumor segmentation obtained after the k-means clustering step (Section 2.6.2). The tumor segmentation (blue lines) of the fusion results obtained from the proposed fusion scheme were compared with those based on the results of the early integration method (red lines). The black lines are the expert delineation, which are used as a ground truth for comparison.

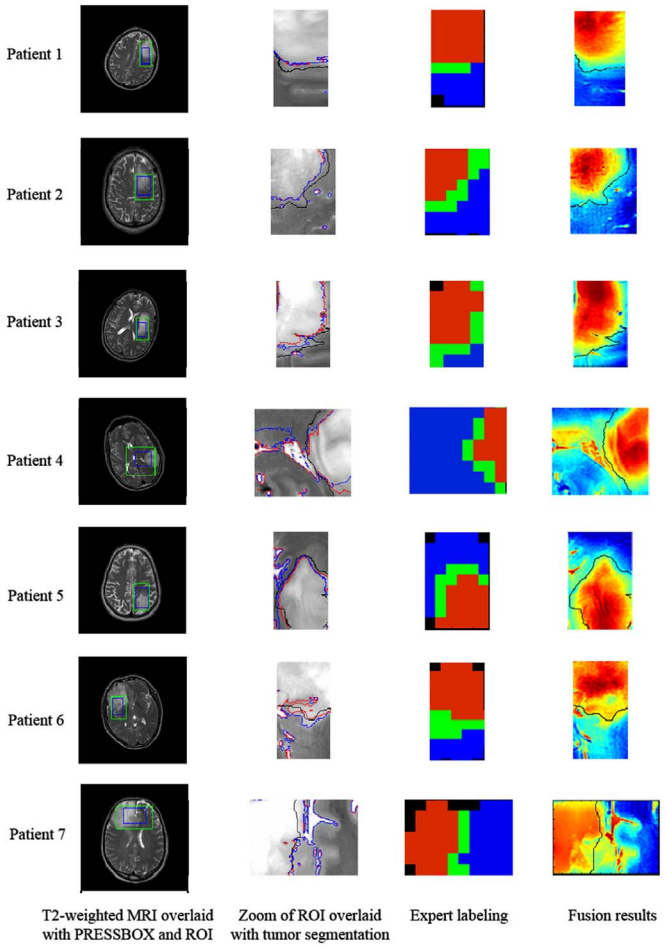


Fig. 3. Fusion results. 1st column: the T2-weighted MRI overlaid with the PRESS box (green box) and the ROI (blue box). 2nd column: the zoom of the ROI (T2-weighted MRI) overlaid with different tumor segmentation lines, blue lines: results of proposed fusion scheme; red lines: results of early integration method; black lines: expert delineation based on conventional MRI. 3rd column: the expert's labeling based on MRSI spectra, blue for normal, red for tumor, green for mixture of normal and tumor tissue and black for voxels of spectral with low quality. 4th column: results of the proposed fusion scheme for tumor distribution. The black lines: the expert delineation of active tumor areas (same as in the 2nd column). (For interpretation of the references to color in this figure legend, the reader is referred to the web version of this article.)

Table 2
Individual result comparison for the tumor source/region.

Patients	Correlation coefficients for feature source ([0–1])		Dice score of tumor region (%)	
	NMF fusion	Early integration	NMF fusion	Early integration
PATIENT 1	**0.91**	0.91	0.92	**0.93**
PATIENT 2	**0.96**	0.92	**0.88**	0.88
PATIENT 3	**0.99**	0.96	**0.87**	0.86
PATIENT 4	**0.91**	0.90	0.72	**0.84**
PATIENT 5	0.94	**0.95**	**0.89**	0.88
PATIENT 6	**0.88**	0.68	**0.93**	0.92
PATIENT 7	**0.99**	0.91	**0.89**	0.89

*Best results within 2 digital numbers are noted using bold numbers.

3.2. Results analysis and methods comparison

Results comparing the proposed method and early integration method with expert labeling are shown in the Table 2. As we can see, the overall results for correlation coefficients of the proposed method are above 0.9 except patient 6. But even for patient 6, the correlation

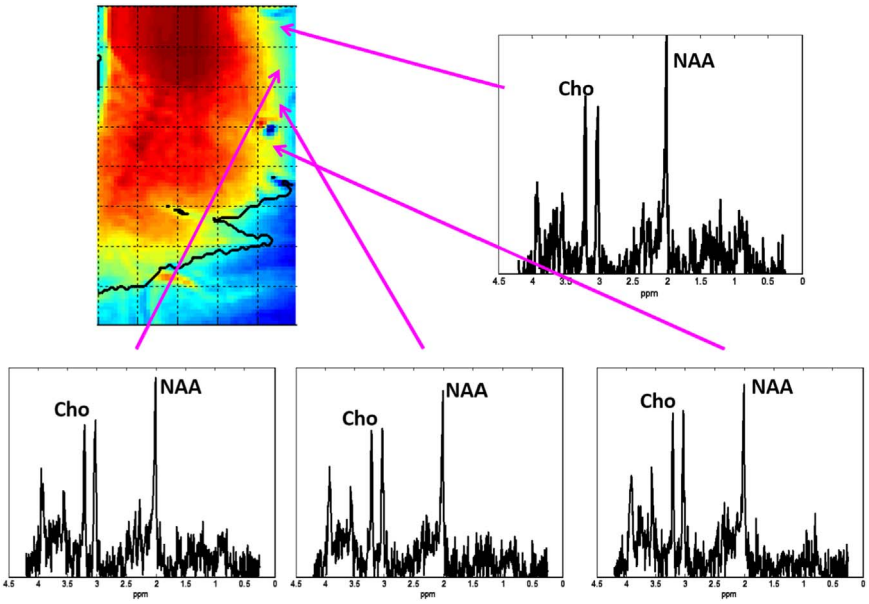


Fig. 4. Spectral investigation of patient 3.

coefficients of the proposed method are still much better than the result of early integration. In general, our fusion method is comparable or outperforms early integration, except for patient 4, which is discussed below.

3.3. Spectral investigation for the conflicting area

As shown in Fig. 3, some results of the tumor's spatial distribution obtained from the proposed method are not consistent with the expert's delineation completely. Hereby, in this section, we further investigate these differences.

For patient 3, four voxels which are delineated as active tumor are illustrated in Fig. 4. Spectra from these voxels show increased Cho peak and decreased NAA peak suggesting tumor infiltration in peri-tumoral regions.

For patient 4, the red region on the left, close to the ventricle, is not within the expert delineation (i.e. the black line). We investigate the MRSI spectra from 6 voxels. As shown in Fig. 5, the spectra from voxel A and voxel D present normal tissue. The red parts mainly come from conventional MRI. But from spectra in voxel B, C, E, and F, we determined a slightly increased Cho peak and the decreased NAA peak in the spectrum from voxel E. However, the spectra are very noisy for this patient, thus the visual assessment might be prone to error.

As shown in Fig. 6, for patient 7, the spectrum from the specific voxel (pointed by the arrow) has shown clearly a decreasing of NAA and an increasing of Cho, which indicate the tumoral infiltration in that area. This also corresponds to the red color presented in that voxel pointed by the arrow. However, the cerebrospinal fluid (CSF) or vessel is also indicated by the red/orange in the middle figure. This is because CSF shows a similar intensity level with the tumor tissue in T2-weighted MRI. Increasing the number of tissue types or including other image modalities may help with reducing this problem.

4. Discussion

4.1. The fusion scheme

The paper proposed a general fusion scheme for MRI and MRSI data which have data structure/dimension and different resolution. Due to these differences, it is impossible to simply borrow or compare with other image fusion methods which are widely used in fusing different MRI scans [35–38]. The “tumor differentiation” in our study

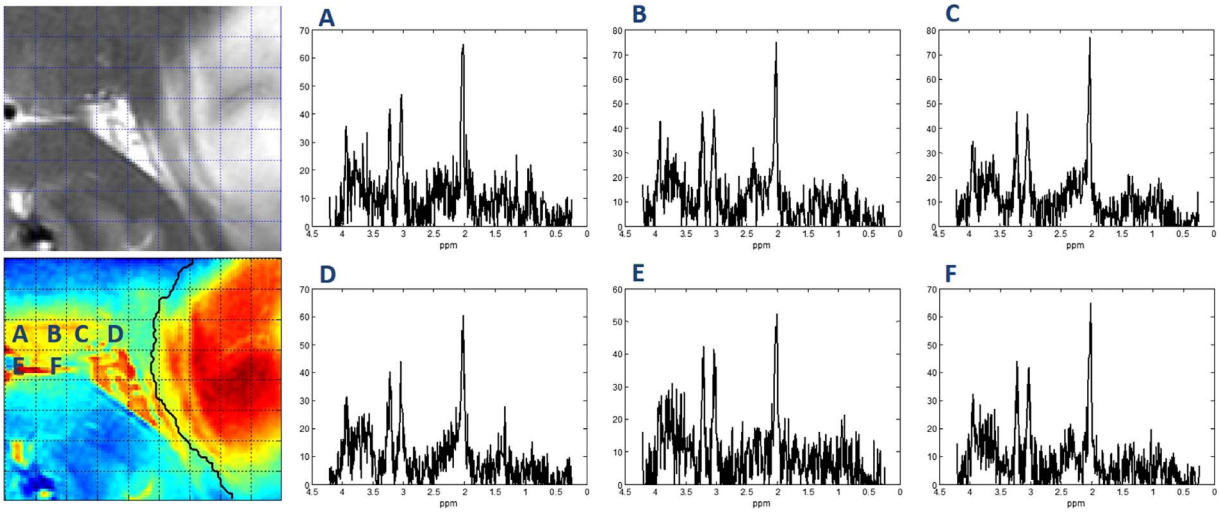


Fig. 5. Spectral investigation of patient 4. (For interpretation of the references to color in this figure, the reader is referred to the web version of this article.)

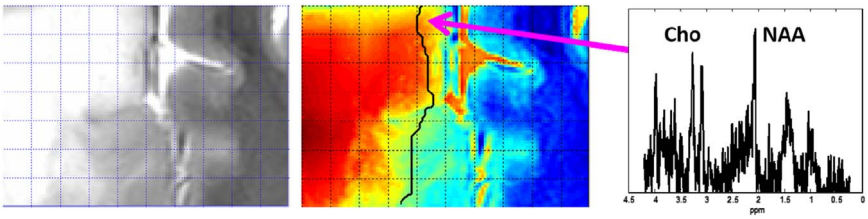


Fig. 6. Spectral investigation of patient 7. (For interpretation of the references to color in this figure, the reader is referred to the web version of this article.)

is different from the concept of "tumor segmentation" using MR images of different scans. Tumor segmentation uses image segmentation methods which focus on creating binary masks or make delineation of particular regions on the image. The focus of our is to develop a fusion scheme that can integrate the conventional MR image into the MRSI-based tumor differentiation. The results of our fusion framework are distribution maps which are represented by different weight values. The k-means clustering for calculating the Dice score is just a trivial step after the tumor distribution map is obtained. It is simply used for binarizing the distribution maps for result validation and can be substituted by any other image segmentation methods.

Under the proposed fusion scheme, we chose HALS [31] as the data decomposition algorithm and wavelet analysis as the image fusion method in our experiments since these two methods shown good results in our previous studies. Other blind source separation methods or image fusion methods may be applicable to enhance performance of the data fusion. Within the NMF inner iteration, the proposed image fusion method based on wavelet decomposition has shown to be a good option. However, other image fusion algorithms which could provide good results may also be used as a substitute. The proposed fusion scheme gives full flexibility of choosing different implementations for its substeps.

Coupled NMF was proposed to generate high-spatial-spectral resolution data using two types of sources: lower-spatial resolution hyperspectral data and lower-spectral resolution multispectral data [27]. Since both of the sources in [27] are spectral data, they were decomposed simultaneously and the spatial information from both types of data was exchanged within each NMF inner iteration. In our case, only the MRSI is multi-dimensional data. MRI considered here is a single high-resolution image. We implemented the NMF decomposition of MRSI data as the main stream of tumor differentiation because more tissue-specific biochemical information is provided by MRSI data. Then the MRSI spatial information updated in each NMF inner iteration is fused with MRI information using wavelet decomposition. Another hot topic in various imaging applications is to fuse a high-resolution panchromatic image with a low-resolution hyperspectral image. Popular methods includes Hue-Intensity-Saturation (HIS) method, principal component analysis (PCA) and High-Pass Filtering (HPF) techniques [39,40]. Recently, a fusion method based on matrix factorization, named the general image fusion (GIF) method, was proposed [41] to reconstruct a very high-resolution hyperspectral image using a lower-resolution hyperspectral image and a high-resolution RGB image. In its fusion scheme, GIF first obtains the spectral source (i.e. the basis) using the spectral data, and then estimates the high-resolution result using the obtained spectral source and the RGB image. Instead of achieving the desired fusion in separated steps, we use a different fusion scheme where the MRSI data decomposition and image fusion are performed simultaneously.

4.2. Image fusion based on wavelet analysis

We implemented wavelet analysis as the image fusion method in our fusion scheme because it has been intensively investigated as a powerful tool for image spatial-frequencies analysis in different scales [42–48]. Popular models for image fusion based on wavelet can be categorized as substitutive models [43], additive models [44], weighted models [45] and some hybrid models [46–48]. Different wavelet-based fusion schemes/models have their advantages and limitations. The choice of models mostly depends on the application. Recently, a successful image fusion method based on wavelet was proposed using CT and MRI for tumor detection [49]. Fusion was performed by taking the absolute maximum of the coefficients to sharpen the features. The experimental results in [49] have also showed that increasing the number of decomposition levels does not necessarily produce better results. This is because overlapping of neighboring features of the lower band signals leads to discontinuities in composite representation and may introduce distortions. Therefore, we used 2 as the number of decomposition levels. This also reduces the computational load of the algorithm. For the wavelet fusion rules, information from MRI and MRSI shows different importance at the high and low frequencies. Therefore, we applied different fusion rules in our fusion scheme. More specifically, we chose the maximum value for high frequencies and calculate the low frequencies using adaptive weights based on Fuzzy Gaussian Membership Function.

4.3. Comparison with tumor differentiation using multi-modality MRI

Sauwen et al. [19] characterized brain tumor tissues with a hierarchical NMF method (hNMF) using multi-parametric MRI, including conventional MRI, perfusion-weighted imaging (PWI), diffusion kurtosis imaging (DKI) and short-TE ^{1}H MRSI as input. Correlation coefficients between computed sources and expert reference sources higher than 0.9 was obtained using this hNMF method. Though good results in differentiating tissue types have been shown, this method is still an early integration method and may be suboptimal in exploiting the intrinsic characteristics of each imaging modality. Our fusion scheme shows better results than those obtained using the early integration fusion scheme as shown in Table 2. Our results are slightly worse than the statistics shown in [19]. This is most likely due to the fact that we have used less modalities (i.e. T2-weighted MRI and MRSI) and lower number of sources which occasionally causes problems such as inclusion of CSF into the tumor delineation. Though our focus is only to propose an efficient scheme for MRSI and MRI data fusion, we can conclude that including other modalities seems beneficial for accurate tumor delineation.

Besides the data modalities, the main difference of the early integration and our method is the fusion scheme. Sauwen et al. [19] stacked the resampled features from all modalities for each voxel and the fusion result was obtained by performing NMF on the stacked features directly. This method treats all the information evenly, without enhancing (i.e., giving a higher weight to) the more relevant features for tumor detection. Instead, we performed the wavelet-based data fusion within each inner iteration of MRSI decomposition. Different weights were considered for data fusion at different frequencies levels according to the characteristics of each data modality. In this way, the fusion procedure is automatically adapted to employ more relevant features at different frequency levels, and thus the tumor detection can be improved.

Tumor segmentation using MR images of different scans is beyond

our discussion. The first reason is that the data structure/dimension is different in our case while the tumor segmentation using different MRI modalities fuses images of the same dimension as discussed in Section 4.1. The second reason is that the aim of our study is also different from tumor segmentation using different MR images. The goal of the latter is to obtain the best tumor segmentation by fusing any image types. Instead, our goal is to improve the resolution of MRSI data in tumor recognition by adding the detail information from high resolution MRI.

5. Conclusions

In this paper, we have proposed a novel fusion scheme based on NMF and wavelet decomposition for brain tumor tissue differentiation. It improves the MRSI resolution and tumor tissue discrimination ability by incorporating detailed information from conventional MRI. At the same time, the bio-chemical information from MRSI data is preserved as much as possible via repeating the image fusion procedure inside NMF inner iteration of MRSI decomposition. Experimental results on in vivo data from low grade glioma patients showed an improvement upon those obtained by performing source separation on stacked features directly. This fusion scheme could be extended to make use of more features from different MR modalities, which might further increase its performance for tumor detection and delineation. The same fusion scheme should also be able to work for high grade glioma, for instance glioblastoma multiforme (GBM), if NMF is performed hierarchically. However, further studies and validation are still needed for investigating the feasibility of the proposed fusion scheme for different data types and for different clinical problems.

Conflicts of interest

The authors declare that there are no conflicts of interest regarding the publication of this paper.

Acknowledgments

This work has been funded by the following projects: National Natural Science Foundation of China (61401068), China Postdoctoral Science Foundation (2014M552341), the Fundamental Research Funds for the Central Universities (ZYGX2014J017, ZYGX2015J007), Flemish Government FWO project G.0869.12N (Tumor imaging); IWT IM 135005; Henri Benedictus Fellowship of the Belgian American Educational Foundation; Interuniversity Attraction Poles Program (P7/11) initiated by the Belgian Science Policy Office. European Research Council under the European Union's Seventh Framework Programme (FP7/2007–2013), ERC Advanced Grant: BIOTENSORS (no. 339804) and the EU MC ITN TRANSACT2012 (no. 316679).

References

[1] B.V. Dasarathy, Editorial: information fusion in the realm of medical applications – a bibliographic glimpse at its growing appeal, Inform. Fusion 13 (1) (2012) 1–9.
[2] S. Van Cauter, F. De Keyzer, D.M. Sima, et al., Integrating diffusion kurtosis imaging, dynamic susceptibility-weighted contrast-enhanced MRI, and short echo time chemical shift imaging for grading gliomas, Neuro-Oncology 16 (7) (2014) 1010–1021.
[3] D.N. Louis, H. Ohgaki, O.D. Wiestler, et al., The 2007 WHO classification of tumours of the central nervous system, Acta Neuropathol. 114 (2007) 97–109.
[4] N.R. Smoll, O.P. Gautschi, B. Schatlo, et al., Relative survival of patients with supratentorial low-grade gliomas, Neuro-Oncology 14 (8) (2012) 1062–1069.
[5] A.H. Jacobs, L.W. Kracht, A. Gossmann, et al., Imaging in neurooncology, NeuroRx 2 (2) (2005) 333–347.
[6] B.L. Dean, B.P. Drayer, C.R. Bird, et al., Gliomas: classification with MR imaging, Radiology 174 (1990) 411–415.
[7] F. Earnest IV, P.J. Kelly, B.W. Scheithauer, et al., Cerebral astrocytomas: histopathologic correlation of MR and CT contrast enhancement with stereotactic biopsy, Radiology 166 (1988) 823–827.
[8] S.J. Nelson, Magnetic resonance spectroscopic imaging, IEEE Eng. Med. Biol. 23 (2004) 30–39.
[9] F.S. De Edelenyi, C. Rubin, F. Esteve, et al., A new approach for analyzing proton magnetic resonance spectroscopic images of brain tumors: nosologic images, Nat. Med. 6 (2000) 1287–1289.
[10] Y. Li, D.M. Sima, S. Van Cauter, et al., Unsupervised nosologic imaging for glioma diagnosis, IEEE Trans. Biomed. Eng. 60 (6) (2013) 1760–1763.
[11] A.W. Simonetti, W.J. Melssen, M. van der Graaf, et al., A chemometric approach for brain tumor classification using magnetic resonance imaging and spectroscopy, Anal. Chem. 75 (20) (2003) 5352–5361.
[12] T. Laudadio, M.C. Martinez-Bisbal, B. Celda, et al., Fast nosological imaging using canonical correlation analysis of brain data obtained by two-dimensional turbo spectroscopic imaging, NMR Biomed. 21 (4) (2008) 311–321.
[13] M. De Vos, T. Laudadio, A.W. Simonetti, et al., Fast nosologic imaging of the brain, J. Magn. Reson. 184 (2) (2007) 292–301.
[14] P. Sajda, S. Du, T.R. Brown, et al., Nonnegative matrix factorization for rapid recovery of constituent spectra inmagnetic resonance chemical shift imaging of the brain, IEEE Trans. Med. Imag. 23 (12) (2004) 1453–1465.
[15] Y. Su, S.B. Thakur, S. Karimi, et al., Spectrum separation resolves partial-volume effect of MRSI as demonstrated on brain tumor scans, NMR Biomed. 21 (2008) 1030–1042.
[16] S. Du, X. Mao, P. Sajda, et al., Automated tissue segmentation and blind recovery of ^{1}H MRS imaging spectral patterns of normal and diseased human brain, NMR Biomed. 21 (2008) 33–41.
[17] S. Ortega-Martorell, P.J.G. Lisboa, A. Vellido, et al., Nonnegative matrix factorisation methods for the spectral decomposition of MRS data from human brain tumours, BMC Bioinformatics 13 (2012) 38.
[18] J. Luts, T. Laudadio, A.J. Idema, et al., Nosologic imaging of the brain: segmentation and classification using MRI and MRSI, NMR Biomed. 22 (4) (2009) 374–390.
[19] N. Sauwen, D.M. Sima, S. Van Cauter, et al., Hierarchical non-negative matrix factorization to characterize brain tumor heterogeneity using multi-parametric MRI, NMR Biomed. 28 (12) (2015) 1599–1624.
[20] X. Liu, Y. Li, Y. Pi, et al., A new algorithm for the fusion of MRSI & MRI on the brain tumour diagnosis, in: Proceedings of ISMRM, Toronto, Canada, 2015.
[21] G. Postma, J. Luts, A. Idema, et al., On the relevance of automatically selected single-voxel MRS and multimodal MRI and MRSI features for brain tumour differentiation, Comput. Biol. Med. 41 (2) (2011) 87–97.
[22] B. Kanberoglu, N.Z. Moore, D. Frakes, et al., Neuronavigation using three-dimensional proton magnetic resonance spectroscopy data, Stereotact. Funct. Neurosurg. 92 (5) (2014) 306–314.
[23] J. Chang, S.B. Thakur, W. Huang, et al., Magnetic resonance spectroscopy imaging (MRSI) and brain functional magnetic resonance imaging (fMRI) for radiotherapy treatment planning of glioma, Technol. Cancer Res. Treat. 7 (5) (2008) 349–362.
[24] E.N. van Lin, J.J. Fütterer, S.W. Heijmink, et al., IMRT boost dose planning on dominant intraprostatic lesions: gold marker-based three-dimensional fusion of CT with dynamic contrast-enhanced and ^{1}H-spectroscopic MRI, Int. J. Radiat. Oncol. 65 (1) (2006) 291–303.
[25] D.D. Lee, H.S. Seung, Learning the parts of objects by non-negative matrix factorization, Nature 401 (1999) 788–791.
[26] Y. Li, D.M. Sima, S. Van Cauter, et al., Hierarchical non-negative matrix factorization (hNMF): a tissue pattern differentiation method for glioblastoma multiforme diagnosis using MRSI, NMR Biomed. 26 (3) (2013) 307–319.
[27] N. Yokoya, Y. Takehisa, I. Akira, Coupled nonnegative matrix factorization unmixing for hyperspectral and multispectral data fusion, IEEE Trans. Geosc. Remote 50 (2) (2012) 528–537.
[28] S. Van Cauter, D.M. Sima, J. Luts, et al., Reproducibility of rapid short echo time CSI at 3 T for clinical applications, J. Magn. Reson. Imaging 37 (2013) 445–456.
[29] R.J. Ogg, P.B. Kingsley, J.S. Taylor, WET, a T1- and B1-insensitive watersuppression method for in vivo localized 1H NMR spectroscopy, J. Magn. Reson. B 104 (1994) 1–10.
[30] J.-B. Poullet, Quantification and classification of magnetic resonance spectroscopic data for brain tumor diagnosis, KU Leuven, Leuven, 2008.
[31] A. Cichocki, R. Zdunek, S. Amari, Hierarchical ALS algorithms for nonnegative matrix and 3D tensor factorization, Lect. Notes Comput. Sci. 4666 (2007) 169–176.
[32] Y. Li, D.M. Sima, S. Van Cauter, et al., Simulation study of tissue type differentiation using non-negative matrix factorization, in: Proceedings of BIOSIGNALS, 2012, pp. 212–217.
[33] S.G. Mallat, A Wavelet Tour of Signal Processing, Academic Press, 1999.
[34] Z. Cui, G. Zhang, J. Wu, Medical image fusion based on wavelet transform and independent component analysis, in: Proceedings of IEEE JCAI, 2009, pp. 480–483.
[35] D. Dera, N. Bouaynaya, H.M. Fathallah-Shaykh, Assessing the non-negative matrix factorization level set segmentation on the BRATS nenchmark, in: Proceedings of BRATS-MICCAI (2016), Athens, Greece, 2016.
[36] K. Kamnitsas, E. Ferrante, S. Parisot, et al., DeepMedic on Brain Tumor Segmentation, in: Proceedings of BRATS-MICCAI (2016), Athens, Greece, 2016.
[37] T.K. Lun, W. Hsu, Brain tumor segmentation using deep convolutional neural network, in: Proceedings of BRATS-MICCAI (2016), Athens, Greece, 2016.
[38] K. Zeng, S. Bakas, A. Sotiras, et al., Segmentation of gliomas in pre-operative and post-operative multimodal magnetic resonance imaging volumes based on a hybrid generative-discriminative framework, in: Proceedings of BRATS-MICCAI (2016), Athens, Greece, 2016.
[39] Z. Wang, Zhijun, D. Ziou, C. Armenakis, et al., A comparative analysis of image fusion methods, IEEE Trans. Geosc. 43 (6) (2005) 1391–1402.
[40] P. Chavez, S.C. Sides, J.A. Anderson, Comparison of three different methods to merge multiresolution and multispectral data-Landsat TM and SPOT panchromatic,, Photogramm. Romote Sens. 57 (3) (1991) 295–303.

[41] R. Kawakami, J. Wright, Y.W. Yu-Wing Tai, et al., High-resolution hyperspectral imaging via matrix factorization in: Proceedings of IEEE CVPR, 2011, pp. 2329–2336.
[42] K. Amolins, Y. Zhang, P. Dare, Wavelet based image fusion techniques—an introduction, review and comparison, Proc. ISPRS J. Photogramm. Romote Sens. 62 (4) (2007) 249–263.
[43] B. Garguet-Duport, J. Girel, J.M. Chassery, et al., The use of multiresolution analysis and wavelets transform for merging SPOT panchromatic and multispectral image data, Photogramm. Romote Sens. 62 (9) (1996) 1057–1066.
[44] M. Gonzalez-Audicana, X. Otazu, O. Fors, et al., Comparison between Mallat's and the 'à trous' discrete wavelet transform based algorithms for the fusion of multispectral and panchromatic images, Int. J. Remote Sens. 26 (3) (2005) 595–614.
[45] T. Ranchin, L. Wald, Fusion of high spatial and spectral resolution images: the ARSIS concept and its implementation, Photogramm. Romote Sens. 66 (1) (2000) 49–61.
[46] Y. Zhang, G. Hong, An IHS and wavelet integrated approach to improve pan-sharpening visual quality of natural colour IKONOS and QuickBird images, Inform. Fusion 6 (3) (2005) 225–234.
[47] M. Gonzalez-Audicana, J.L. Saleta, R.G. Catalan, et al., Fusion of multispectral and panchromatic images using improved IHS and PCA mergers based on wavelet decomposition, IEEE Trans. Geosc. Remote 42 (6) (2004) 1291–1299.
[48] X. Otazu, M. Gonzalez-Audicana, O. Fors, et al., Introduction of sensor spectral response into image fusion methods. Application to wavelet-based methods, IEEE Trans. Geosc. Remote 43 (10) (2005) 2376–2385.
[49] V. Angoth, C.Y.N. Dwith, A. Singh, A novel wavelet based image fusion for brain tumor detection, Int. J. Comput. Vis. Signal Process 2 (1) (2013) 1–7.